Journal of Materials Chemistry A

PAPER

View Article Online
View Journal | View Issue

Cite this: J. Mater. Chem. A, 2015, 3, 9682

Electrode activation *via* vesiculation: improved reversible capacity of γ-Fe_2O_3@C/MWNT composite anodes for lithium-ion batteries†

Yongfei Liu,*[a] Junmin Xu,[b] Xiaoying Qin,*[a] Hongxing Xin,[a] Xueqin Yuan,[a] Jian Zhang,[a] Di Li[a] and Chunjun Song[a]

Received 28th January 2015
Accepted 23rd March 2015

DOI: 10.1039/c5ta00701a

www.rsc.org/MaterialsA

Capacity fading caused by pulverization is the basic issue for transition-metal-oxide anodes in lithium-ion batteries (LIBs). Here we report a simple and scalable fabrication of core–shell structured γ-Fe_2O_3@C nanoparticle based composites incorporated with multi-walled carbon nanotubes (MWNTs), through a vacuum-carbonization of the synthesized metal–organic complex and MWNT hybrids. In the constructed γ-Fe_2O_3@C/MWNT architecture, the carbon shell layers can not only buffer the volume change of γ-Fe_2O_3 nanoparticles but also improve their conductivity; while the flexible and conductive MWNT networks can maintain the structural and electrical integrity of the electrodes during the charge/discharge cycles. As a result, such γ-Fe_2O_3@C/MWNT electrodes, tested as anodes for LIBs, exhibit excellent cycling performance with monotonically increased reversible capacities along with cycles. For instance, the specific capacity rises at a rate of ~6.8 mA h g^{-1} per cycle to 1139 mA h g^{-1} after 60 cycles at the current density of 100 mA g^{-1}. Such electrode activation was revealed to be closely related to the increased active surface area of the electrode arising from the gradual vesiculation in Fe_2O_3@C nanoparticles during lithiation/delithiation in the as-prepared robust γ-Fe_2O_3@C/MWNT architecture.

Introduction

Rechargeable lithium-ion batteries (LIBs) are increasingly used in portable electronics, electric vehicles, and other applications.[1–4] Since the commercial graphite anode material has already approached its theoretical limit (372 mA h g^{-1}),[5] it is urgent nowadays to seek alternative anode materials with a high reversible capacity and a long lifetime. In this context, Fe_2O_3-based materials have emerged as promising candidates for next generation LIB anodes because of their high theoretical capacity (1007 mA h g^{-1}), low cost, and environmental acceptance. However, Fe_2O_3 electrodes suffer from poor electrical conductivity and poor cycle performance with large capacity fading because of pulverization caused by the drastic volume change during the charge/discharge process,[6,7] which hinder its practical applications in LIBs. Several strategies have been proposed to overcome these drawbacks and further enhance the structural stability of the Fe_2O_3-based materials. One approach is to increase the effective contact area between the active materials and the electrolyte by designing nanostructure and hierarchical micro/nanostructures, or controlling pore structures, such as using α-Fe_2O_3 nanoflakes,[8] α-Fe_2O_3 nanorods,[9] Fe_2O_3 microboxes,[10] spindle-like mesoporous α-Fe_2O_3 particles,[11] which can reduce the path lengths for the transport of electrons and lithium ions. Another approach is to use hybrid electrodes composed of Fe_2O_3 and carbon materials, such as single-walled carbon nanohorns/α-Fe_2O_3 composites,[12] reduced graphene oxide/Fe_2O_3 composites,[13] and Fe_2O_3/CNT/graphene hybrid materials,[14] which can effectively improve the conductivity and fast charge/discharge rates of the electrodes. Meanwhile, these carbon materials can also accommodate the mechanical strain of lithium ion insertion/extraction much better than the bare Fe_2O_3 electrode materials. These strategies inspire us to rationally design and synthesize an anode material system with unique structures to enhance their electrochemical performance.

As we know, the capacity of lithium storage for Fe_2O_3 anodes is mainly achieved through the reversible conversion reaction between Li^+ and Fe_2O_3 active materials.[8] Recent studies have noticed that interfacial lithium storage generally takes place as a result of the electrochemical reaction at the interface of active materials, in which a gradually increased capacity is exhibited during the initial several cycles.[11,15] However, the detailed activation mechanism involved is not yet fully understood,[15] and the relationship between electrode activation and microstructure evolution with cycles has also not been deeply studied. On the other hand, although α-Fe_2O_3 materials have been widely investigated as anodes for LIBs nowadays,[8–17] only a few studies

[a]Key Laboratory of Materials Physics, Institute of Solid State Physics, Chinese Academy of Sciences, Hefei 230031, P R China. E-mail: log1218@163.com; xyqin@issp.ac.cn
[b]High Magnetic Field Laboratory, Chinese Academy of Sciences, Hefei 230031, P R China

† Electronic supplementary information (ESI) available: Experimental details and characterization: Fig. S1–S4. See DOI: 10.1039/c5ta00701a

were performed on the electrochemical performance of γ-Fe_2O_3 anode materials.[18,19] Lee *et al.* fabricated γ-Fe_2O_3/carbon microparticles through a hydrothermal method followed by chemical vapor deposition. They obtained a specific capacity of 900 mA h g^{-1} after 40 cycles at 100 mA g^{-1} when tested as an anode.[18] Vargas and co-workers reported the hydrothermal synthesis of γ-Fe_2O_3/graphene nanosheet composites, which retained a reversible capacity of 429 mA h g^{-1} after 100 cycles at 1000 mA g^{-1}.[19] Very recently, Natelson's group showed that a composite material made of graphene nanoribbons and γ-Fe_2O_3 nanoparticles could exhibit a high discharge capacity of ~910 mA h g^{-1} after 134 cycles at 100 mA g^{-1}.[20] Despite the progress achieved to date, the research studies on the facile and scalable synthesis of γ-Fe_2O_3-based materials with a high specific capacity and a long lifetime are still in a very early stage.

Herein, we report the fabrication of core–shell structured γ-Fe_2O_3@C nanoparticle based composites incorporated with multi-walled carbon nanotubes (MWNTs). When tested as anodes for LIBs, such γ-Fe_2O_3@C/MWNT electrodes exhibit excellent cycling performance and monotonically elevated reversible capacity. For instance, their capacity rises at a rate of ~6.8 mA h g^{-1} per cycle to 1139 mA h g^{-1} after 60 cycles, as the charge/discharge current density is equal to 100 mA g^{-1}; or their capacity rises at a rate of ~2.0 mA h g^{-1} per cycle to 723 mA h g^{-1} after 200 cycles at the current density of 1000 mA g^{-1}. By *ex situ* high-resolution transmission electron microscopy (HRTEM) examinations, we show that the core–shell structured γ-Fe_2O_3@C nanoparticles transform into a vesiculate structure without pulverization during the cyclic charge/discharge. As the vesiculate structure develops, the core–shell structured γ-Fe_2O_3@C/MWNT anodes are gradually activated. It was revealed that the activation of the electrode is closely related to the increase of the active surface area arising from the gradual formation of the vesiculate structure.

Experimental

Synthesis of γ-Fe_2O_3@C/MWNT composites

The reagents were obtained from commercial sources and used without further purification. The γ-Fe_2O_3@C/MWNT composite was synthesized through a carbonization of the hybrid of metal–organic complexes and MWNTs. Typically, terephthalic acid (PTA, 3.99 g), $LiOH \cdot H_2O$ (2.01 g), and MWNTs (0.63 g) were dissolved and dispersed in 500 mL of warm ionized water (60 °C) with supersonic treatment for 30 min. Then 6.66 g of $FeSO_4 \cdot 7H_2O$ was added into the mixed solution with stirring for 24 h to form the hybrid of ferrous benzoate and MWNTs. After filtering, the as-prepared precursors were vacuum sealed in a quartz tube and calcined at 500 °C for 4 h. Then the obtained powders were further annealed at 200 °C for 24 h in air to form the γ-Fe_2O_3@C/MWNT composites (Fig. 1a). For comparison, core–shell structured γ-Fe_2O_3@C nanoparticles were also prepared in the absence of MWNTs.

Characterization

Scanning electron microscopy (SEM) investigations were conducted on a FEI Sirion 200 field emission SEM. TEM and HRTEM experiments were performed on a JEOL JEM-2010 TEM. Powder X-ray diffraction (XRD) was conducted on a Panalytical X'Pert Pro MPD X-ray diffractometer using Cu Kα radiation (λ = 1.54 Å). X-Ray photoelectron spectroscopy (XPS) analysis was conducted on a VG ESCALAB Mark II X-ray photoelectron spectroscope. Thermogravimetric analysis (TGA) was conducted on a Perkin-Elmer Pyris 1 thermogravimetric analyzer at a heating rate of 10 °C min^{-1} from 25 °C to 700 °C in air flow.

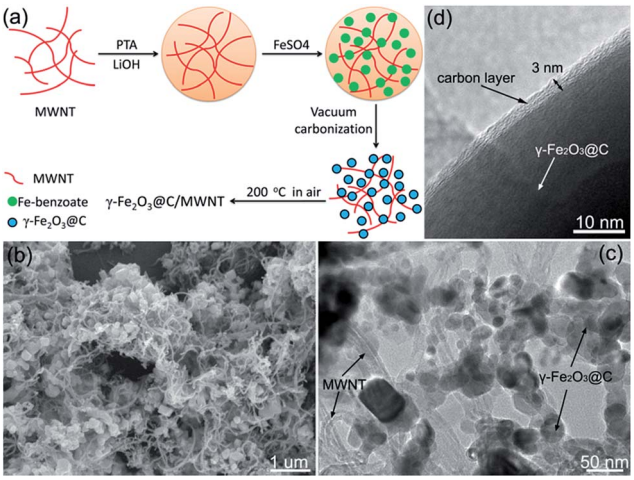

Fig. 1 (a) Schematic illustration of the preparation of γ-Fe_2O_3@C/MWNT. (b) SEM and (c) TEM images of γ-Fe_2O_3@C/MWNT. (d) TEM image of a γ-Fe_2O_3@C particle.

Battery fabrication and electrochemical measurement

Scanning the electrodes were done through a standard procedure as follows: active materials (γ-Fe_2O_3@C/MWNT and γ-Fe_2O_3@C composites), super-P carbon black, and polyvinylidene fluoride (PVDF), in a weight ratio of 7 : 2 : 1 were blended in *N*-methylpyrrolidone (NMP) to form a homogenous slurry. Electrodes were prepared by coating the slurry on copper foil and then vacuum-dried at 120 °C for 12 h. Standard CR2032 coin cells were assembled in an Ar-filled glove box, using lithium foil as the counter electrode, 1 M $LiPF_6$ in ethylene carbonate/dimethyl carbonate/diethyl carbonate (1 : 1 : 1 by volume) as the electrolyte, and Celgard 2325 as the separator. Cyclic voltammetry (CV) measurement was conducted at 0.2 mV s^{-1} in the range of 0–3.0 V on a CHI660C electrochemical workstation. The electrochemical impedance spectroscopy (EIS) of the cells was evaluated in the frequency range from 0.01 Hz to 100 kHz at the Zahner Zennium electrochemistry workstation. Discharge/charge measurements of the cells were performed between the potential range of 0.01–3.0 V (*vs.* Li/Li^+) under a Neware BTS TC53 battery test system. All of the specific capacities were calculated on the basis of the total weight of the γ-Fe_2O_3@C/MWNT or γ-Fe_2O_3@C composites.

Results and discussion

As shown in Fig. 1a, the synthetic protocol of the γ-Fe_2O_3@C/MWNT composite is mainly composed of two steps. First, the

ferrous benzoate and MWNT composites were synthesized by a modified procedure based on the reported work.[21] In this synthesis, the introduced $LiOH \cdot H_2O$ provided an alkaline condition to dissolve PTA into the ionized water, which facilitated the next reaction. In the second step, after vacuum annealing, the as-prepared ferrous benzoate precursor was converted to γ-Fe_2O_3 nanoparticles capsulated by a carbon layer, while the MWNT network still remained, thus leading to the formation of γ-Fe_2O_3@C/MWNT composites.

Fig. 1b shows a typical SEM image of the as-prepared γ-Fe_2O_3@C/MWNT composites. Evidently, a large number of dispersed particles of ~100 nm in size are distributed homogeneously in the 3D MWNT networks. The corresponding TEM images reveal that these nanoparticles are composed of agglomerated nanograins with sizes ranging from ~10 to 50 nm and entangled with MWNT networks (Fig. 1c), and the carbon shell layer encapsulating around the core is ~3 nm in thickness (Fig. 1d). It should be emphasized that the addition of MWNTs in the synthesis is favorable for forming robust hybrid nanoarchitectures, but does not affect the formation of core–shell structured γ-Fe_2O_3@C nanoparticles, which can also form in the absence of MWNTs (see ESI Fig. S1a–c†).

XRD patterns of the samples are shown in Fig. 2a. All the peaks of the Fe_2O_3@C powders can be indexed to γ-Fe_2O_3 with a cubic phase (JCPDS card no. 39-1346). No obvious peaks of carbon were detected, indicating the amorphous attribute of the carbon shell layer. In comparison, the XRD pattern of the γ-Fe_2O_3@C/MWNT shows an additional peak at 26°, which can be attributed to the (002) plane of the graphitic structure contributed from the MWNTs. HRTEM images of the γ-Fe_2O_3@C nanoparticle clearly demonstrate that the γ-Fe_2O_3 nanoparticle is highly crystallized and the carbon shell presents the amorphous state (see Fig. S1c†), highly in agreement with the XRD result. The lattice fringe images (see Fig. S1c and d†) reveal the clear core interfringe distance of 0.48 nm and the nanotube interfringe distance of 0.33 nm, which are in good agreement with that of the (111) plane of γ-Fe_2O_3 and the (002) plane of MWNTs, respectively.

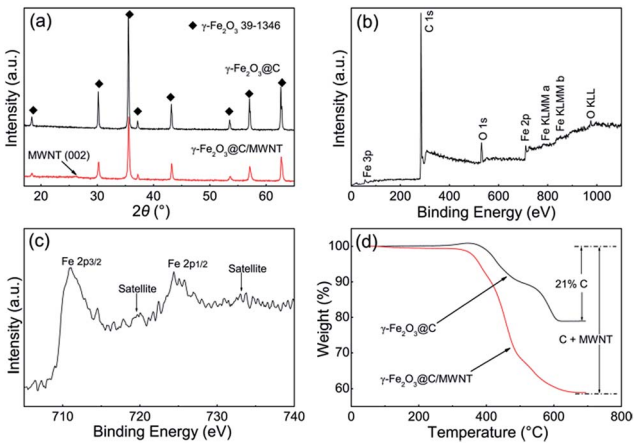

Fig. 2 (a) XRD patterns of the composites; (b) and (c) XPS spectra of the γ-Fe_2O_3@C/MWNT composite; (d) TG curves of the composites.

In order to further confirm that the synthesized iron oxide cores are maghemite (γ-Fe_2O_3), an XPS examination was performed. The typical survey spectrum shows the presence of Fe, C, and O elements in the γ-Fe_2O_3@C/MWNT composite (Fig. 2b). The high-resolution spectrum of Fe reveals that, in contrast to the Fe_3O_4 XPS spectrum, it contains the charge transfer satellites of Fe $2p_{3/2}$ and Fe $2p_{1/2}$ at 720 eV and 732 eV, respectively, which indicate the absence of Fe^{2+}, confirming that the core is maghemite (γ-Fe_2O_3).[22,23] Furthermore, TGA was used to reveal the precise chemical composition of the composites (as shown in Fig. 2d). The results show that γ-Fe_2O_3@C nanoparticles have a chemical composition of 79 wt% γ-Fe_2O_3 and 21 wt% C, and the γ-Fe_2O_3@C/MWNT composites have a chemical composition of 59 wt% γ-Fe_2O_3, 15.7 wt% C, and 25.3 wt% MWNTs (based on the consideration that the ratio of γ-Fe_2O_3 to the carbon layer is unchanged).

To measure the electrochemical performance of the as-prepared composites, CR2032 coin cells were fabricated according to a widely reported procedure.[24,25] Their charge storage behaviors were first characterized by cyclic voltammetry (CV). Fig. S2a† shows the representative CV curves of the γ-Fe_2O_3@C electrode at room temperature between 0 and 3.0 V at a scan rate of 0.2 mV s^{-1}. In the first discharge cycle, a well-defined cathodic peak at 0.44 V can be observed clearly, which is usually ascribed to the formation of a solid electrolyte interphase (SEI) layer and the complete reduction of Fe_2O_3 to Fe.[25] This peak disappears in the subsequent cycles, while three weak peaks at 0.78, 0.96, and 1.2 V appear, indicating the occurrence of an irreversible phase transformation during the lithiation/delithiation process in the first cycle.[8,16] During the charge process, a broad anodic peak composed of two peaks (at 1.68 and 1.96 V) are observed, corresponding to the oxidative reactions of Fe^0 to Fe^{2+} and Fe^{2+} to Fe^{3+}, respectively, highly in accord with the electrochemical process of α-Fe_2O_3-based anodes.[17,26] The γ-Fe_2O_3@C/MWNT composite shows similar CV characteristics (see Fig. S2b†).

As shown in Fig. 3a and b, the charge/discharge profiles for the γ-Fe_2O_3@C and γ-Fe_2O_3@C/MWNT electrodes are also very similar. A potential plateau appears at ~0.75 V during the first discharge process, which represents the reduction of Fe_2O_3 to form nano-sized Fe^0 and an amorphous Li_2O matrix.[8] The initial discharge and charge capacities are 1091 and 666 mA h g^{-1} for γ-Fe_2O_3@C, and 1523 and 857 mA h g^{-1} for γ-Fe_2O_3@C/MWNT, corresponding to irreversible capacity losses of ~39% and ~43%, respectively. Such high capacity losses may be ascribed to the inevitable formation of the SEI layer and the decomposition of the electrolyte, which is usually observed in Fe-based anode materials.[11] This characteristic is also in agreement with the CV results that the intense cathodic peak at 0.44 V that existed in the first scan is absent afterward (see Fig. S2†). The discharge voltage plateau at ~0.75 V in the first cycle is different from those in other cycles afterward at ~1.0 V (Fig. 3a and b), further indicating that irreversible reactions occurred in the first cycle.[26]

The cycling performances of the two electrodes are shown in Fig. 3c at a current density of 100 mA g^{-1} from 3.0 to 0.01 V. The core–shell structured γ-Fe_2O_3@C nanoparticle electrode

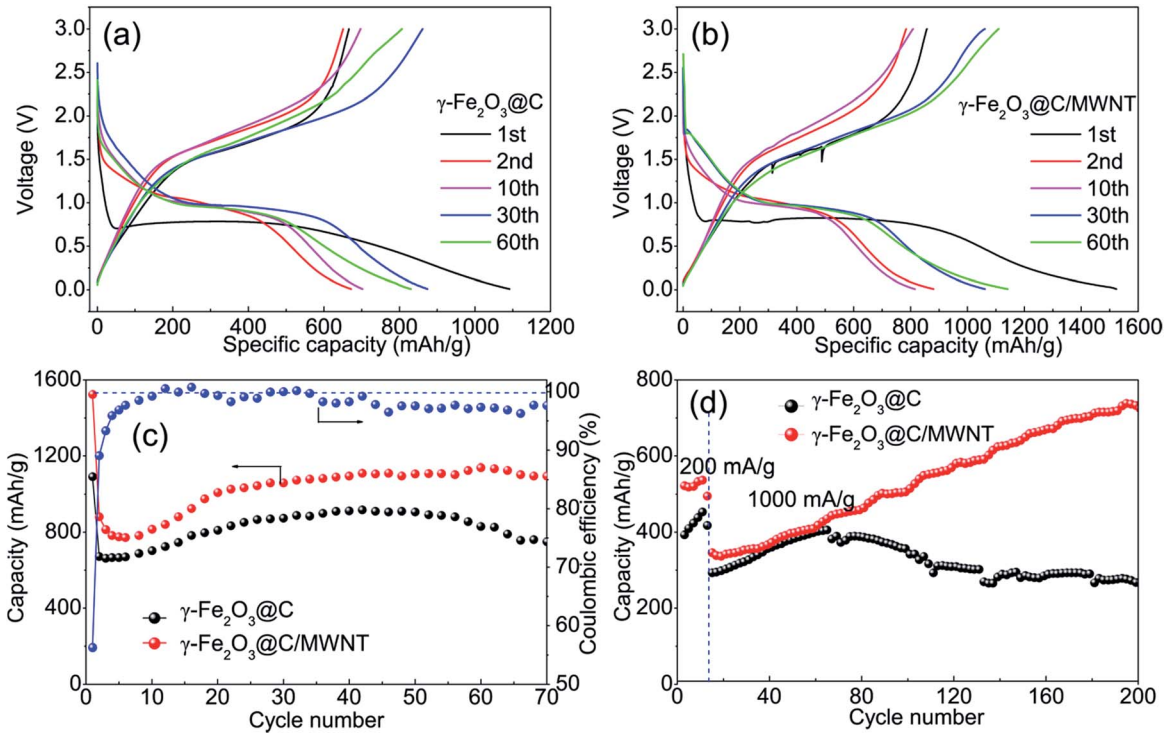

Fig. 3 Charge/discharge voltage curves of (a) γ-Fe_2O_3@C and (b) γ-Fe_2O_3@C/MWNT electrodes at a current density of 100 mA g^{-1}. Cycling performances and Coulombic efficiencies of the electrodes at the current densities of (c) 100 mA g^{-1} and (d) 1000 mA g^{-1}.

demonstrates a gradually increased discharge capacity up to 906 mA h g^{-1} after 50 cycles. While the as-prepared γ-Fe_2O_3@C/MWNT composite electrode delivers higher discharge capacities, increasing at a rate of ~6.8 mA h g^{-1} per cycle to 1139 mA h g^{-1} after 60 cycles, much higher than that of the γ-Fe_2O_3@C electrode, indicating a significant enhancement in the cycling performance due to the introduction of MWNTs. This value is also higher than the theoretical capacity of γ-Fe_2O_3 (1007 mA h g^{-1}), such high capacity should be ascribed to the interfacial (surface) Li storage *via* a pseudo-capacitive mechanism.[27–29] The Coulombic efficiencies for the γ-Fe_2O_3@C/MWNT electrode rapidly increase from 56.3% for the first cycle to about 99% after ten cycles and remain over 97% thereafter (as shown in Fig. 3c), which suggests a facile lithium insertion/extraction.[30] In order to further confirm the advantages of this γ-Fe_2O_3@C/MWNT composite in lithium storage, the capacities of the two electrodes have been investigated upon 200 cycles at the rate of 1000 mA g^{-1} and the cycling performances are displayed in Fig. 3d. Thirteen cycles were first performed at 200 mA g^{-1} and then 187 cycles at 1000 mA g^{-1}. One can see that the reversible capacity for the γ-Fe_2O_3@C electrode first rises to 400 mA h g^{-1} within 65 cycles and then decreases to 265 mA h g^{-1} at the 200th cycle, while that for the γ-Fe_2O_3@C/MWNT electrode rises steadily at a rate of ~2.0 mA h g^{-1} per cycle from the initial 350 mA h g^{-1} to 723 mA h g^{-1} after 200 cycles. In addition, the electrochemical performance of pure MWNTs is also examined for comparison. As shown in Fig. S3,† one can find that the specific discharge capacities of the MWNTs decrease gradually during the initial several cycles and then stabilize at about 200 mA h g^{-1}. This is much lower than the reversible capacities of the γ-Fe_2O_3@C electrode, indicating that the capacity enhancement (γ-Fe_2O_3@C *vs.* γ-Fe_2O_3@C/MWNT, as shown in Fig. 3c and d) is due to the synergistic effect of γ-Fe_2O_3@C nanoparticles and MWNTs. The superior cycling stability of the γ-Fe_2O_3@C/MWNT electrode should be attributed to the flexible and conductive MWNTs. One can see that lots of cracks exist in the cycled γ-Fe_2O_3@C anode, while no obvious cracks can be observed in the cycled γ-Fe_2O_3@C/MWNT anode (see Fig. S4†). This result indicates that the addition of MWNTs can not only accommodate the mechanical stress induced by the volume change of the γ-Fe_2O_3@C nanoparticles, but also inhibits the breakdown of the electrical connection of the γ-Fe_2O_3@C nanoparticles from the anode and thus maintains the structural and electrical integrity of the electrode during the cyclic charge/discharge processes. Such cycling stability at low and high charge/discharge rates are significantly higher than previously reported works on carbon coated porous γ-Fe_2O_3 microparticles (900 mA h g^{-1} after 40 cycles at 100 mA g^{-1})[18] and γ-Fe_2O_3/graphene nanosheet composites (429 mA h g^{-1} after 100 cycles at 1000 mA g^{-1}).[19]

It is noteworthy that both of the two electrodes show increased capacities at different current densities during the first dozens even hundreds of cycles, implying a gradual activation of the electrodes. A similar phenomenon was also reported for the bare α-Fe_2O_3 electrode, which exhibited a discharge capacity rise (~6%) during the initial several cycles.[11] It was ascribed to the reversible formation of a gel-like layer generated from the electrolyte decomposition or further

interfacial lithium storage as a result of the electrochemical reaction at the interface of active materials.[11,15,31] However, for our γ-Fe_2O_3@C/MWNT electrode, the percentages of the increase of the capacity are up to ~48% (from 770 to 1139 mA h g^{-1} at the current density of 100 mA g^{-1}) and ~106% (from 350 to 723 mA h g^{-1} at the current density of 1000 mA g^{-1}), respectively, which are not common in the reported various nanostructured metal oxide electrodes.[7,32–36]

To clarify the mechanism of this activation of the electrodes, the CV test was performed for a γ-Fe_2O_3@C/MWNT electrode after different cycles at 100 mA g^{-1}. As shown in Fig. 4a, one can see that the intensity of the anodic peak (i_{pa}) at ~1.8 V and the integral area of the curve (corresponding to the capacity) rise gradually along with the charge/discharge cycles, suggesting that the electrode has been gradually activated and forms a more stable structure, which is capable of withstanding the volume change. According to the Randles–Sevcik equation,[37] the peak current can be described as follows:

$$i_{pa} = (2.69 \times 10^5) n^{3/2} A C D^{1/2} v^{1/2} \quad (1)$$

where n is the electron stoichiometry during the oxidation/redox reaction, A is the active surface area of the electrode, C is the concentration of the diffusing species, D is the diffusion coefficient of Li^+, and v is the voltage scan rate. For our solid state γ-Fe_2O_3@C/MWNT electrodes, the n value is constant during the cycles, and the C value can also be considered to be unchanged due to the excess of the solid lithium counter electrode. Hence, the rise of i_{pa} indicates a gradual increase of A and/or D along with the charge/discharge cycles, which should be closely related to the microstructure evolution of the active materials.

In this context, *ex situ* TEM and HRTEM analyses of the electrodes were performed to examine their structural changes along with the cycles (Fig. 5). During the initial several cycles (Fig. 5a–c), the TEM images show that the dense Fe_2O_3 nanoparticles have progressively transformed to the vesiculate structure, which should originate from the aggregation of the vacancies produced during the extraction of Li, as revealed in the dealloying for Li-alloying anodes.[38–40] The HRTEM image reveals that the Fe_2O_3 particle still possesses a relatively integrated microstructure with a distinct lattice fringe (Fig. 5e). After 50 cycles, the Fe_2O_3 particles become more loose and porous due to the formation of larger pores at the expense of small pores (Fig. 5d). The corresponding HRTEM image as

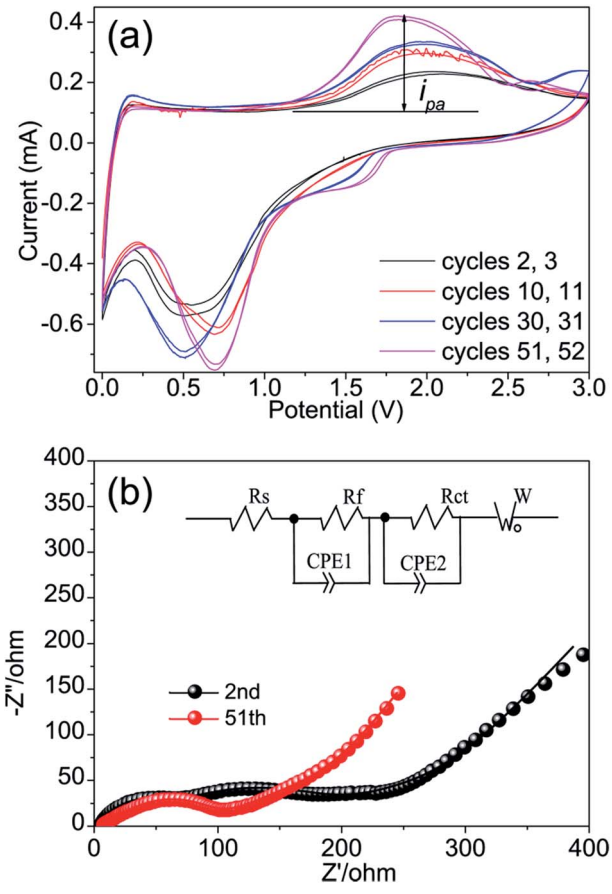

Fig. 4 (a) Representative CV curves of a γ-Fe_2O_3@C/MWNT electrode after different cycles and (b) Nyquist plots (Z' *vs.* $-Z''$) of the 2nd and 51st cycles of the γ-Fe_2O_3@C/MWNT electrode. Symbols represent experimental data and continuous lines represent fitted data using the equivalent electrical circuit of the inset of (b).

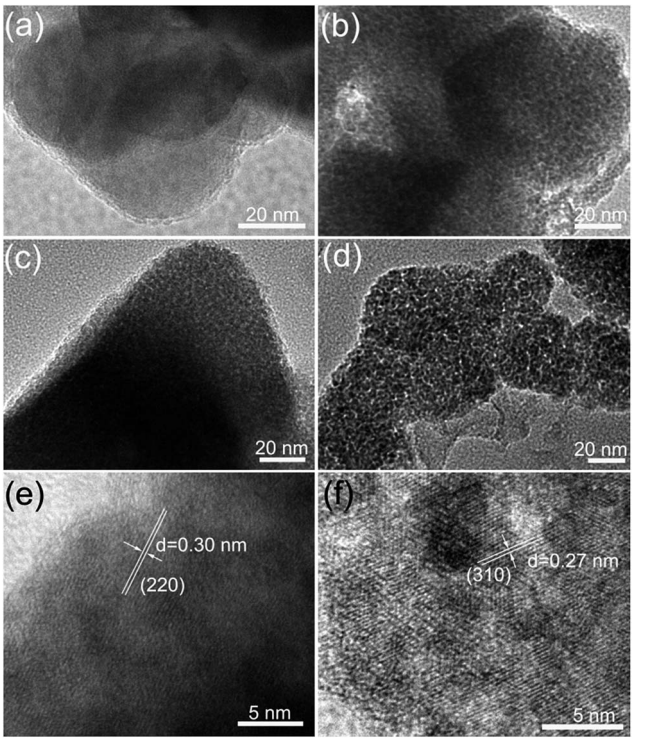

Fig. 5 TEM and HRTEM images showing the structure evolution of the γ-Fe_2O_3@C particles with the lithiation/delithiation cycles: (a) 0 cycle, (b) 1 cycle, (c and e) 5 cycles, and (d and f) 50 cycles. All of the cycled electrodes are sampled from the cells in a fully charged status. A vesiculate structure of the γ-Fe_2O_3@C particle was gradually formed during the cycles. The interplanar distances of the selected areas are calculated to be 0.30 and 0.27 nm, which agree with the (220) and (310) planes of γ-Fe_2O_3, respectively.

revealed in Fig. 5f indicates that the Fe_2O_3 nanoparticle has transformed to clusters composed of some small nano-domains with almost common crystallographic orientation. Hence, one can conclude that the considerable interface including the surfaces of the pores and the interface within the clusters form after the cyclic charge/discharge, which are active sites for further interfacial lithium storage.[11,15,41] Meanwhile, in contrast with the well crystallized zones in the Fe_2O_3 nanoparticles, the formed vesiculate structure and the interface (the domain boundaries with the clusters) can also serve as the tunnel for Li^+ transport, leading to a faster diffusion of Li ions. As a result, both the active surface area and the diffusion coefficient increase, highly in agreement with the CV analyses (Fig. 4a). It is worth noting that although the vesiculate structure forms, no pulverization is observed from the TEM investigation, which should be due to the protection of the capsulated carbon shell around the Fe_2O_3 nanoparticles.[5,26] This vesiculate mesoporous structure can provide a large number of interfaces for the interfacial Li storage, leading to a high reversible capacity (1139 mA h g^{-1}, as shown in Fig. 3c) beyond the theoretical capacity.

Furthermore, electrochemical impedance spectroscopy (EIS) was conducted at frequencies from 100 kHz to 0.01 Hz to understand the effect of the structure evolution of the active materials on their electrochemical performances. The EIS data were analysed by fitting to an equivalent electrical circuit shown in the inset of Fig. 4b. It consists of the electrolyte (R_s), surface film (R_f), and charge transfer (R_{ct}) resistances, two constant phase elements (CPE_1 and CPE_2), and a diffusional component Warburg impedance (W). As shown in Fig. 4b, the Nyquist plots for the 2nd and 51st cycles are similar, exhibiting a high-frequency depressed semicircle (corresponding to R_f) and a medium-frequency depressed semicircle (corresponding to R_{ct}) followed by a linear tail (corresponding to W) in the low-frequency region.[42] The resistance values after curve fitting are listed in Table 1. One can see that the R_f of the 51st cycle is significantly lower than that of the 2nd cycle. Generally, the increased active surface area upon cycling may lead to the increasing SEI layer, and thus increase the R_f. However, for our core–shell structured γ-Fe_2O_3@C material, the SEI layer formed in the first cycle will shield the vesiculate electrode from the erosion of the electrolyte during the next cycles. In other words, despite the increased active surface area within the γ-Fe_2O_3@C nanoparticle upon cycling, no extra SEI layer forms within the γ-Fe_2O_3@C nanoparticles. Hence, the R_f would not increase, but will slightly decrease due to the partial decomposition of the outer SEI layer,[41] leading to the decrease of R_f. The change of R_{ct} from 123.2 to 50.9 Ω suggests a significant reduce of charge transfer resistance after cycling, which should be attributed to the formation of the vesiculate structure. The increase of the active surface area arising from such a structure evolution of the electrode can lead to rapid electron transport during the electrochemical lithium insertion/extraction reaction, and thus result in significant improvement on the cycling performance. This result suggests that it is effective to improve the electrochemical performance of metal oxides through the electrode vesiculation.

Table 1 Impedance parameters of the cell, with γ-Fe_2O_3@C/MWNT as the cathode and a Li-metal anode, during the 2nd and 51st discharge/charge cycles at ~1.0 V

Parameter	R_s/Ohm	R_f/Ohm	R_{ct}/Ohm
2nd cycle	3.6	45.9	123.2
51st cycle	5.1	33.1	50.9

Conclusions

To summarize, γ-Fe_2O_3@C/MWNT nanocomposites have been successfully fabricated by a facile and scalable synthesis method in combination with a vacuum-carbonization process. The γ-Fe_2O_3@C/MWNT electrodes deliver increased specific capacities along with cycles, which are closely related to the increased effective active surface area and the porous structure during the vesiculation of the electrode, and the robust structure composed of 3D MWNT networks and γ-Fe_2O_3@C nanoparticles. Considering the low cost, environmental acceptance, and large-scale production of the γ-Fe_2O_3@C/MWNT in the present work, such anode materials hold great potential for practical applications in lithium ion batteries.

Acknowledgements

This work was supported in part by the National Natural Science Foundation of China (no. 11374306, no. 11174292, no. 50972146, and no. 10904144).

Notes and references

1 X. Li, X. Meng, J. Liu, D. Geng, Y. Zhang, M. N. Banis, Y. Li, J. Yang, R. Li, X. Sun, M. Cai and M. W. Verbrugge, *Adv. Funct. Mater.*, 2012, **22**, 1647–1654.
2 X. Li, A. Dhanabalan, L. Gu and C. Wang, *Adv. Energy Mater.*, 2012, **2**, 238–244.
3 Y. Zhao, X. Li, B. Yan, D. Li, S. Lawes and X. Sun, *J. Power Sources*, 2015, **274**, 869–884.
4 X. Li and C. Wang, *J. Mater. Chem. A*, 2013, **1**, 165–182.
5 W.-M. Zhang, X.-L. Wu, J.-S. Hu, Y.-G. Guo and L.-J. Wan, *Adv. Funct. Mater.*, 2008, **18**, 3941–3946.
6 P. L. Taberna, S. Mitra, P. Poizot, P. Simon and J. M. Tarascon, *Nat. Mater.*, 2006, **5**, 567–573.
7 P. Poizot, S. Laruelle, S. Grugeon, L. Dupont and J. M. Tarascon, *Nature*, 2000, **407**, 496–499.
8 M. V. Reddy, T. Yu, C. H. Sow, Z. X. Shen, C. T. Lim, G. V. Subba Rao and B. V. R. Chowdari, *Adv. Funct. Mater.*, 2007, **17**, 2792–2799.
9 Y.-M. Lin, P. R. Abel, A. Heller and C. B. Mullins, *J. Phys. Chem. Lett.*, 2011, **2**, 2885–2891.
10 L. Zhang, H. B. Wu, S. Madhavi, H. H. Hng and X. W. Lou, *J. Am. Chem. Soc.*, 2012, **134**, 17388–17391.
11 X. Xu, R. Cao, S. Jeong and J. Cho, *Nano Lett.*, 2012, **12**, 4988–4991.

12 Y. Zhao, J. Li, Y. Ding and L. Guan, *Chem. Commun.*, 2011, **47**, 7416–7418.
13 X. Zhu, Y. Zhu, S. Murali, M. D. Stoller and R. S. Ruoff, *ACS Nano*, 2011, **5**, 3333–3338.
14 S. Q. Chen, P. Bao and G. X. Wan, *Nano Energy*, 2013, **2**, 425–434.
15 Z. Wang, D. Luan, S. Madhavi, Y. Hu and X. W. Lou, *Energy Environ. Sci.*, 2012, **5**, 5252–5256.
16 B. Sun, J. Horvat, H. S. Kim, W.-S. Kim, J. Ahn and G. Wang, *J. Phys. Chem. C*, 2010, **114**, 18753–18761.
17 G. Zhou, D.-W. Wang, P.-X. Hou, W. Li, N. Li, C. Liu, F. Li and H.-M. Cheng, *J. Mater. Chem.*, 2012, **22**, 17942–17946.
18 Y. Ma, G. Ji and J. Y. Lee, *J. Mater. Chem.*, 2011, **21**, 13009–13014.
19 O. Vargas, A. Caballero and J. Morales, *Electrochim. Acta*, 2014, **130**, 551–558.
20 J. Lin, A.-R. O. Raji, K. Nan, Z. Peng, Z. Yan, E. L. G. Samuel, D. Natelson and J. M. Tour, *Adv. Funct. Mater.*, 2014, **24**, 2044–2048.
21 Q. Zhu, F. Tao and Q. Pan, *ACS Appl. Mater. Interfaces*, 2010, **2**, 3141–3146.
22 M. Descostes, F. Mercier, N. Thromat, C. Beaucaire and M. Gautier-Soyer, *Appl. Surf. Sci.*, 2000, **165**, 288–302.
23 Y. Liu, L. Yu, Y. Hu, C. Guo, F. Zhang and X. Wen Lou, *Nanoscale*, 2012, **4**, 183–187.
24 X. L. Jia, Z. Chen, X. Cui, Y. T. Peng, X. L. Wang, G. Wang, F. Wei and Y. F. Lu, *ACS Nano*, 2012, **6**, 9911–9919.
25 Y. Z. Wu, P. B. Zhu, M. V. Reddy, B. V. R. Chowdari and S. Ramakrishna, *ACS Appl. Mater. Interfaces*, 2014, **6**, 1951–1958.
26 C. He, S. Wu, N. Zhao, C. Shi, E. Liu and J. Li, *ACS Nano*, 2013, **7**, 4459–4469.
27 J. Y. Shin, D. Samuelis and J. Maier, *Adv. Funct. Mater.*, 2011, **21**, 3464–3472.
28 E. Z. Liu, J. M. Wang, C. S. Shi, N. Q. Zhao, C. N. He, J. J. Li and J. Z. Jiang, *ACS Appl. Mater. Interfaces*, 2014, **6**, 18147–18151.
29 X. Wang, L. Qiao, X. Sun, X. Li, D. Hu, Q. Zhang and D. He, *J. Mater. Chem. A*, 2013, **1**, 4173–4176.
30 W. Chen, Z. Zhang, W. Bao, Y. Lai, J. Li, Y. Gan and J. Wang, *Electrochim. Acta*, 2014, **134**, 293–301.
31 W.-J. Yu, P.-X. Hou, F. Li and C. Liu, *J. Mater. Chem.*, 2012, **22**, 13756–13763.
32 Y. Shi, B. Guo, S. A. Corr, Q. Shi, Y.-S. Hu, K. R. Heier, L. Chen, R. Seshadri and G. D. Stucky, *Nano Lett.*, 2009, **9**, 4215–4220.
33 Z. Wang, J. S. Chen, T. Zhu, S. Madhavi and X. W. Lou, *Chem. Commun.*, 2010, **46**, 6906–6908.
34 Y. Yu, C. H. Chen and Y. Shi, *Adv. Mater.*, 2007, **19**, 993–997.
35 S.-H. Lee, Y.-H. Kim, R. Deshpande, P. A. Parilla, E. Whitney, D. T. Gillaspie, K. M. Jones, A. H. Mahan, S. Zhang and A. C. Dillon, *Adv. Mater.*, 2008, **20**, 3627–3632.
36 H.-X. Zhang, C. Feng, Y.-C. Zhai, K.-L. Jiang, Q.-Q. Li and S.-S. Fan, *Adv. Mater.*, 2009, **21**, 2299–2304.
37 C. Comminges, R. Barhdadi, M. Laurent and M. Troupel, *J. Chem. Eng. Data*, 2006, **51**, 680–685.
38 T. Kennedy, E. Mullane, H. Geaney, M. Osiak, C. O'Dwyer and K. M. Ryan, *Nano Lett.*, 2014, **14**, 716–723.
39 J. Erlebacher, M. J. Aziz, A. Karma, N. Dimitrov and K. Sieradzki, *Nature*, 2001, **410**, 450–453.
40 X. H. Liu, S. Huang, S. T. Picraux, J. Li, T. Zhu and J. Y. Huang, *Nano Lett.*, 2011, **11**, 3991–3997.
41 P. Balaya, H. Li, L. Kienle and J. Maier, *Adv. Funct. Mater.*, 2003, **13**, 621–625.
42 Q. Zhang, T. Peng, D. Zhan and X. Hu, *J. Power Sources*, 2014, **250**, 40–49.